PHYSICAL REVIEW B **89**, 035439 (2014)

Signature of the topological surface state in the thermoelectric properties of Bi_2Te_3

F. Rittweger,[1] N. F. Hinsche,[2,*] P. Zahn,[3] and I. Mertig[1,2]
[1]*Max-Planck-Institut für Mikrostrukturphysik, Weinberg 2, DE-06120 Halle, Germany*
[2]*Institut für Physik, Martin-Luther-Universität Halle-Wittenberg, DE-06099 Halle, Germany*
[3]*Helmholtz-Zentrum Dresden-Rossendorf, P. O. Box 51 01 19, DE-01314 Dresden, Germany*
(Received 18 July 2013; revised manuscript received 5 December 2013; published 31 January 2014)

We present *ab initio* electronic structure calculations based on density functional theory for the thermoelectric properties of Bi_2Te_3 films. Conductivity and thermopower are computed in the diffusive limit of transport based on the Boltzmann equation. Bulk and surface contributions to the transport coefficients are separated by a special projection technique. As a result we show clear signatures of the topological surface state in the thermoelectric properties.

DOI: 10.1103/PhysRevB.89.035439 PACS number(s): 71.15.Mb, 73.50.Lw, 72.20.−i, 03.65.Vf

Recent studies in condensed-matter physics showed that Bi_2Te_3, which is one of the most studied and efficient thermoelectric materials [1,2], belongs to the group of $Z2$ topological insulators [3–5]. Clearly the link between an efficient thermoelectric material and its topological character is the spin-orbit-induced inverted band gap. While the small size of the band gap favours room-temperature thermoelectrics [6], the inversion itself is often triggered by heavy atoms, leading to low lattice thermal conductivity, enhancing the figure of merit. In addition, the existence of topological surface states opens the opportunity to increase the performance of thermoelectric devices [7–9].

While many experiments and calculations have been performed investigating the robustness and the spin texture of the gapless surface state in Bi_2Te_3 [5,10,11], the precise identification of the surface states' contribution to the various transport coefficients is still an open question [12,13]. We present *ab initio* calculations of the thermoelectric transport properties of a Bi_2Te_3 film. The transport properties of the Bi_2Te_3 film are calculated in the diffusive limit of transport by means of the semiclassical Boltzmann equation in the relaxation-time approximation (RTA) [14–20]. Within this approximation we assume that the attached metallic leads basically preserve the surface band structure.

The electronic structure of the Bi_2Te_3 surface was obtained by first-principles density functional theory (DFT) calculations, as implemented in the fully relativistic screened Korringa-Kohn-Rostoker Green function method [21]. Exchange and correlation effects were accurately taken into account by the local density approximation parametrized by Vosko, Wilk, and Nusair [22]. The atomistic structure was simulated by a slab configuration of 20 atomic layers of Bi_2Te_3, i.e., four quintuple layers (QLs), separated by a vacuum spacer of sufficient thickness to separate the films. The experimental in-plane lattice parameter $a_{\mathrm{BiTe}}^{\mathrm{hex}} = 4.384$ Å and relaxed atomic positions [23] were used. The calculated electronic band structure of the Bi_2Te_3 surface (black dots) is shown together with the projected bulk band structure (gray shaded areas) along the hexagonal high-symmetry lines in Fig. 1(a). The findings are in good agreement with previous calculations [24–26]. The Dirac point of the Bi_2Te_3 gapless surface state is located deep inside the bulk valence bands, at about 168 meV below the bulk valence-band maximum (VBM), clearly reinforced by the distinct indirect bulk band gap. As is known from theory [27] and experiment [28,29] the hybridization of the surface states localized on both sides of the slab leads to an artificial band gap opening of the Dirac state on the order of a few meV. We observed a closure of the Dirac-point band gap within an accuracy of 1 meV for 6 QLs, albeit not showing any influence on the states' character or the transport properties of the surface states.

With increasing Fermi level starting at the Dirac point the Fermi surface is circular, becoming hexagonal at ≈150 meV [cf. Figs. 1(c) and 1(d)] and getting snowflakelike above 270 meV [Fig. 1(b)]. The origin of warping is the hybridization of the surface state with the bulk states in the $\bar{\Gamma}\bar{M}$ direction above 252 meV giving rise to a flat energy band, while in the $\bar{\Gamma}\bar{K}$ direction the surface state stays isolated from the bulk states up to 0.8 eV. The Fermi velocities in the high-symmetry directions differ remarkably, by $v_{\mathrm{F}}^{\bar{\Gamma}\bar{M}}/v_{\mathrm{F}}^{\bar{\Gamma}\bar{K}} \approx 0.4$, over a large energy range $E_{\mathrm{F}} - E_{\mathrm{D}} \approx 0.25 - 0.5$ eV.

The DFT results serve as input to obtain the thermoelectric transport properties, using the layer-resolved transport distribution function (TDF) $\Sigma_{\parallel,i}(\mu) = \mathcal{L}_{\parallel,i}^{(0)}(\mu,0)$ [30,31]. The generalized conductance moments $\mathcal{L}_{\parallel,i}^{(n)}(\mu,T)$ are defined as

$$\mathcal{L}_{\parallel,i}^{(n)}(\mu,T) = \frac{\tau_{\parallel}}{(2\pi)^2} \sum_{\nu} \int d^2\boldsymbol{k} \left|v_{\boldsymbol{k},(\parallel)}^{\nu}\right|^2 \mathcal{P}_{\boldsymbol{k}}^{i} \left(E_{\boldsymbol{k}}^{\nu} - \mu\right)^n \left(-\frac{\partial f_{(\mu,T)}}{\partial E}\right)_{E=E_{\boldsymbol{k}}^{\nu}}. \tag{1}$$

$v_{\boldsymbol{k},(\parallel)}^{\nu}$ denote the group velocities in the directions of the hexagonal basal plane and $\mathcal{P}_{\boldsymbol{k}}^{i}$ is the layer-resolved probability amplitude of a Bloch state defined as

$$\int d\boldsymbol{r} |\mathring{\psi}_{\boldsymbol{k}}(\boldsymbol{r})|^2 = \sum_i \mathcal{P}_{\boldsymbol{k}}^{i} = 1. \tag{2}$$

Here the relaxation time for Bi_2Te_3 was fitted to experimental data and chosen to be constant in its absolute value $\tau = 11$ fs with respect to wave vector $\boldsymbol{k}$ and energy on the scale of $k_{\mathrm{B}}T$ [20]. No distinction of surface and bulk scattering was assumed to allow for a clear discussion of the effect of electronic

---

[*] nicki.hinsche@physik.uni-halle.de

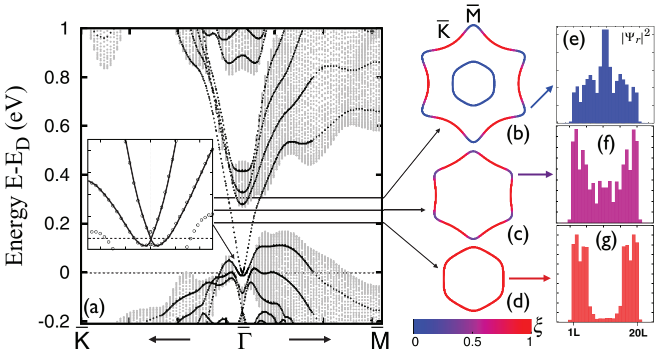

FIG. 1. (Color online) (a) Band structure of the 30-layer Bi_2Te_3 slab (black dots) and surface-projected bulk band structure (gray shaded areas). As an inset the surface Dirac state is highlighted. The Fermi surface at (b) 316 meV, (c) 270 meV and (d) 205 meV above the Dirac energy E_D is shown. Superimposed onto the Fermi surfaces is the probability density (e)–(g) of the surface states. Red color indicates a pure surface state mostly localized in the outermost quintuple layers, as shown in (g). Blue color refers to bulklike contributions to the surface states along the $\bar{\Gamma}\bar{M}$ high-symmetry line, as presented in (e) and (f).

structure on the electronic transport. The influence of electron-phonon coupling was theoretically and experimentally found to be very weak and is discussed in more detail in the Appendix. It is straightforward to obtain the temperature- and doping-dependent in-plane electrical conductivity $\sigma_{\parallel}$ and thermopower $S_{\parallel}$ as

$$\sigma_{\parallel} = 2e^2 \mathcal{L}_{\parallel}^{(0)}(\mu,T) \quad \text{and} \quad S_{\parallel} = \frac{1}{eT} \frac{\mathcal{L}_{\parallel}^{(1)}(\mu,T)}{\mathcal{L}_{\parallel}^{(0)}(\mu,T)} \tag{3}$$

for given chemical potential μ at temperature T and carrier concentration n.[1]

All transport calculations presented below are performed with adaptive k-point meshes larger than 500 points on a piece of the two-dimensional (2D) Fermi surface which lies in the irreducible part of the Brillouin zone (BZ) and at least 150 000 (56×10^6 k points) k points in the entire 3D BZ for the bulk TDF at large (small) charge carrier concentrations. Detailed descriptions were given in earlier publications [32,33]. By means of the layer-resolved probability amplitude $\mathcal{P}_{\boldsymbol{k}}^{i}$ the thermoelectric transport properties can be decomposed into contributions of typical eigenstates. Here, the distinction between surface states, characterized by a strong spatial localization in the outermost QL together with an exponential decay into the bulk and vacuum, and bulk states is required. This is done by probing a test eigenstate $\mathring{\psi}_{\boldsymbol{k}}(\boldsymbol{r})$ with the prototype surface eigenstate $\psi_{\boldsymbol{k},\text{SS}}(\boldsymbol{r})$ via $\xi_{\boldsymbol{k}} = \int d\boldsymbol{r}\psi^{*}_{\boldsymbol{k},\text{SS}}(\boldsymbol{r})\mathring{\psi}_{\boldsymbol{k}}(\boldsymbol{r})$. If $\xi_{\boldsymbol{k}}$ is larger than a given threshold close to 1,[2] the state $\boldsymbol{k}$ is considered a surface state. An example for the latter is given in Fig. 1(g), showing the layer-resolved probability amplitude. Most of the surface states' probability amplitude is located at the outermost QL [34]. Furthermore, the information about the states' character is shown on the Fermi surfaces in Figs. 1(b)–1(d). It is seen that all states of the surface band crossing the band gap possess surface state character with the corresponding spatial distribution [Fig. 1(d)] up to an energy of about 220 meV above the Dirac point. From here, slight deviations of the state's prototype surface state character occur [cf. Fig. 1(f)], as states in the $\bar{\Gamma}\bar{M}$ direction start to show hybridization between bulk and surface states. We note that these changes start well below the bulk conduction-band edge, $E_{\text{CBM}} - E_{\text{F}} \approx 20$ meV. At elevated energies the states in the $\bar{\Gamma}\bar{M}$ direction show clear bulklike character with a high probability amplitude in the center of the layer, as shown, e.g., in Fig. 1(e). Consequently, $\xi_{\boldsymbol{k}} \rightarrow 0$ and these states do not behave as typical surface states, although originating from the Dirac band. As indicated earlier the surface states' band is unaffected by hybridization effects in the $\bar{\Gamma}\bar{K}$ direction up to $E_{\text{F}} - E_{\text{D}} \approx 0.8$ eV. As a result the Fermi surface shows emerging bulk or surface character, most convincingly depicted in Fig. 1(b). As will be discussed hereinafter, this fact leads to a strong influence on the electronic transport, indicating an exceptional almost constant electrical surface conductivity over a broad doping regime.

The basis of all transport properties discussed below is the TDF $\Sigma_{\parallel}(\mu)$, which can be understood as the electrical conductivity at vanishing temperature. Due to hybridization, the TDF of the surface states contains contributions from surface and bulk states, which can be clearly separated using the projection technique by the probability amplitudes as introduced above. We will distinguish between contributions from the pure surface state (SS) [cf. Fig. 1(g)], located at the surface, and bulk contributions to the surface states. The bulk TDF (gray shaded areas) as well as the surface (red solid line) contribution of the TDF are shown in Fig. 2. The TDF of the surface contribution rises almost linearly with energy. Having in mind that for a two-dimensional system the TDF scales as $\Sigma_{\parallel}(\mu) \propto dl_{\text{F}} v_{\parallel}$, where dl_{F} is the length of the Fermi circle at chemical potential μ, the linearity of the TDF in energy close to the Dirac point is obvious. Here, $v_{\parallel}$

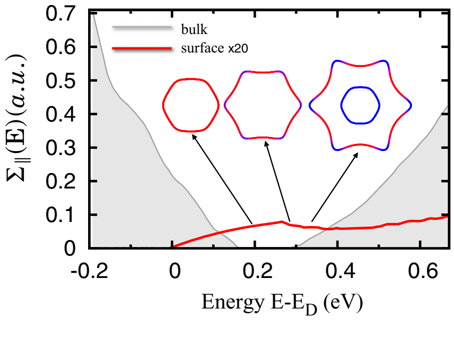

FIG. 2. (Color online) Transport distribution function $\Sigma_{\parallel}(E)$ of the bulk and surface states of Bi_2Te_3. The red solid line refers to the contribution to $\Sigma_{\parallel}(E)$ of mainly the outermost quintuple layers [cf. Fig. 1(g)]. The gray shaded area indicates the pure bulk contribution to $\Sigma_{\parallel}(E)$. Note that the surface contributions are multiplied by a factor of 20. The inset shows the corresponding Fermi surfaces as a function of energy [cf. Figs. 1(b)–1(d)].

---

[1] The fixed charge N at varying $\mu(T)$ is determined by an integration over the density of states $g(E)$, $N = \int_{\mu-\Delta E}^{\text{VBM}} dE\, g(E)[f(\mu,T) - 1] + \int_{\text{CBM}}^{\mu+\Delta E} dE\, g(E) f(\mu,T)$.

[2] Throughout this study a threshold of 0.90 was used.

is constant with energy, while $dl_{\rm F} \propto E$. Small deviations from the latter arise about $E_{\rm F} - E_{\rm D} \approx 0.1$ eV and can be related to the hexagonal warping of the Fermi surface. At about 250 meV the increase of the TDF saturates and $\Sigma_{\parallel}^{\rm SS}$ remains roughly constant over a wide range of energy. As pointed out earlier, the pure surface states not only are spatially confined within approximately the outermost QL, but are also restricted to selected $\boldsymbol{k}$ directions because of the hybridization with the bulk states. In the ultimate limit of $\boldsymbol{k}$ selection only one Bloch function in the $\bar{\Gamma}\bar{K}$ direction with a constant Fermi velocity $v_{\rm F}^{\bar{\Gamma}\bar{K}}$ approximately realized for energies up to 0.8 eV above the Dirac point would be available for each surface state. As a consequence, the TDF of the surface state reads

$$\Sigma_{\rm 1D}(\mu) = \frac{1}{\pi}\int dk \big(v_{\rm F}^{\bar{\Gamma}\bar{K}}\big)^2 \delta\big(\mu - v_{\rm F}^{\bar{\Gamma}\bar{K}} k\big) = \frac{L v_{\rm F}^{\bar{\Gamma}\bar{K}}}{\pi}. \qquad (4)$$

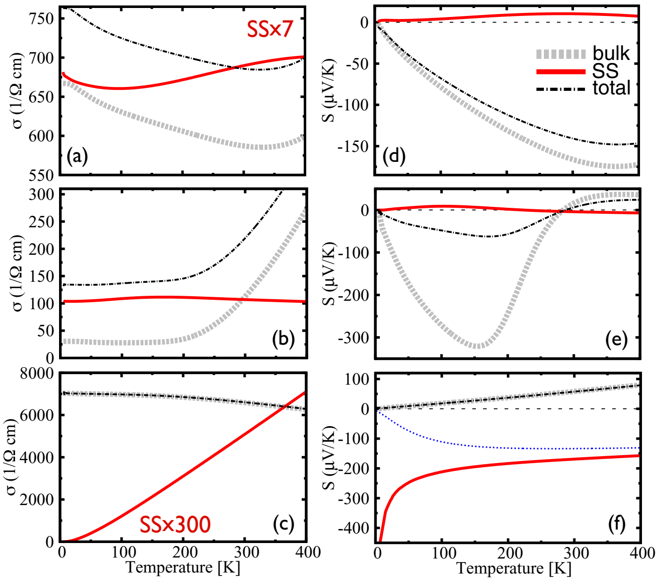

FIG. 3. (Color online) Electrical conductivity (a)–(c) and thermopower (d)–(f) in dependence on temperature for three distinct charge carrier concentrations. (a),(d) electron charge carrier concentration of $n = 2 \times 10^{19}$ cm^{-3}, (b),(e) electron charge carrier concentration of $n = 1 \times 10^{18}$ cm^{-3}, and (c),(f) hole charge carrier concentration of $p = 4 \times 10^{20}$ cm^{-3}. Pure bulk contributions are indicated by gray dashed lines, the contribution of the surface states is given by red solid lines, while black dash-dotted lines show the total contribution of the half-infinite sample. In (f) the contribution of the surface state to the thermopower at $p = 3 \times 10^{20}$ cm^{-3} is given additionally (blue thin dotted line), to emphasize the thermodynamical limit of the thermopower at vanishing temperature. Further details can be found in the text.

Obviously, the transition from the two-dimensional character of the surface states into a one-dimensional one changes the energy dependence of the TDF from linear into a constant (cf. Fig. 2). With the TDF being directly related to $\mathcal{L}_{\parallel}^{(0)}(\mu,T)$ the electrical conductivity of the surface state is expected to be energy independent for electron doping as well. We note that the fact of the Dirac point being buried deep inside the bulk valence bands causes a surface contribution to the TDF only for energies larger than $E_{\rm D}$. In the following, we will discuss the doping- and temperature-dependent electrical conductivity and thermopower, as shown in Fig. 3. As we did before, we will distinguish between contributions from bulk states (gray dashed lines), surface states (red solid lines), and the total contribution (black dash-dotted line), defined as $\sigma_{\rm tot} = \sigma_{\rm bulk} + \sigma_{\rm SS}$ and $S_{\rm tot} = (\sigma_{\rm bulk} S_{\rm bulk} + \sigma_{\rm SS} S_{\rm SS})/\sigma_{\rm tot}$. Three typical charge carrier concentrations are chosen to reflect the overall behavior of the transport properties. Due to the mere fact that a three-dimensional topological insulator offers robust metal-like surface states in the insulating bulk band gap, an enhanced electrical conductivity of the whole system is expected for very small charge carrier concentrations, i.e., when the chemical potential is situated in the bulk band gap. The temperature dependence of the electrical conductivity for such a scenario, at an electron doping of $n = 1 \times 10^{18}$ cm^{-3}, is shown in Fig. 3(b). The surface contribution $\sigma_{\rm SS}$ of the electrical conductivity is almost temperature independent at approximately 105 $(\Omega\,{\rm cm})^{-1}$ for the entire temperature range. This behavior is a consequence of the earlier discussed energy independence of the TDF for electron doping. For low temperatures $\sigma_{\rm SS}$ is up to four times larger than the bulk value of 28 $(\Omega\,{\rm cm})^{-1}$ and the surface conductivity clearly dominates. For elevating temperatures bipolar bulk conduction leads to the well-known exponential increase in $\sigma_{\rm bulk}$ for narrow-band-gap semiconductors and $\sigma_{\rm bulk} > \sigma_{\rm SS}$ holds for $T > 300$ K. Due to the lack of dependence of $\sigma_{\rm SS}$ on temperature, the surface contribution to the total electrical conductivity is almost hidden and causes a notable offset only at low temperatures. However, such a behavior was experimentally seen for thin $\rm Bi_2Te_3$ films [13,35]. It might be possible to experimentally clarify whether surface states contribute to the total transport or not by measuring the total thermopower $S_{\rm tot}$ of the system, which decomposed into its parts is shown in Fig. 3(e). For the bulk contribution of $S_{\rm tot}$ the typical behavior for a slightly doped narrow-band-gap bulk semiconductor is obtained. With increasing temperature the absolute value of $S_{\rm bulk}$ rises linearly and the chemical potential shifts from the bulk conduction band into the bulk band gap. At a temperature of about 155 K large bulk values of the thermopower of $-320\ \mu$V/K are obtained. At higher temperatures $S_{\rm bulk}$ saturates at the expected small values because of bipolar intrinsic transport. For a bulk semiconductor in the intrinsic limit $S_{\rm max} \sim \frac{E_{\rm G}(T_{\rm max})}{2T_{\rm max}}$ holds. The surface contribution $S_{\rm SS}$ shows the expected metal-like behavior with absolute values well below $\pm 10\ \mu$V/K. This leads in sum to a clearly diminished total thermopower. More precisely, assuming that $S_{\rm bulk} \gg S_{\rm SS}$, $S_{\rm tot} \approx S_{\rm bulk}/(\eta + 1)$ for $\eta = \sigma_{\rm SS}/\sigma_{\rm bulk}$. The maximal absolute value of the total thermopower [black dash-dotted line in Fig. 3(e)] is found to be reduced to one-fifth of the bulk value; it is $-62\ \mu$V/K at 170 K, which corroborates the above-noted estimation. We note that within the RTA, the signature of the surface state on $S_{\rm tot}$ depends on the ratio of the relaxation times, i.e., $\tau_{\rm SS}/\tau_{\rm bulk}$. If $\tau_{\rm bulk} \gg \tau_{\rm SS}$ the reduction of the total thermopower due to the conducting surface state will be much weaker than proposed. However, the opposite scenario $\tau_{\rm SS} \gg \tau_{\rm bulk}$ should be expected, considering the backscattering protection of the surface state [12,36]. Overall, a clear transport contribution of the surface state will lead to a heavily decreased absolute value of the total thermopower.

To complete the picture two additional doping regimes will be discussed. Usually bulk Bi_2Te_3 is intrinsically electron doped due to antisite defects [37]. In Figs. 3(a) and 3(d) the electron doping amounts to $n = 2 \times 10^{19}$ cm^{-3} and μ lies in or close to the bulk conduction band. Here σ_{tot} is mainly defined by the bulk conductivity and reaches 685 $(\Omega\,\text{cm})^{-1}$ at room temperature. The surface contribution is about 12%–15% for all temperatures, being almost constant with temperature, again reflecting the weak energy dependence of the TDF. With the surface thermopower, as expected, behaving metallically, but $\sigma_{\text{bulk}} \gg \sigma_{\text{SS}}$, the surface states' impact on S_{tot} is only moderate, reducing S_{tot} just to 15% of the bulk value.

Recent model calculations [8,9] for Bi_2Te_3 proposed a dramatically enhanced thermoelectric power factor, i.e., $S\sigma^2$, at low temperatures and a location of the chemical potential near the Dirac point. To enter this regime, high hole doping rates are necessary. Here, we fixed the hole charge carrier concentration to $p = 4 \times 10^{20}$ cm^{-3} to discuss a possible enhancement of the thermoelectric power factor of Bi_2Te_3 in the presence of gapless metal-like surface states. Indeed, as is shown in Fig. 3(f), S_{SS} possesses large semiconductorlike absolute values, even showing a divergence for $T \to 0$, with $\mu(T = 0)$ coinciding with the Dirac energy E_{D}. This behavior originates in the asymmetric slope of the TDF, imitating a bulk band edge and yielding $S_{\text{SS}} \sim -1/(\mu - E_{\text{D}})$.[3] Nevertheless the total thermopower and the bulk contribution to the thermopower are identical, both showing small positive values and a linear temperature dependence as expected from a highly doped hole semicondcutor. The reason is the heavily suppressed contribution of the surface states due to the large difference between σ_{SS} and σ_{bulk} as shown in Fig. 3(c). With the chemical potential deep in the bulk valence bands near the Dirac point, σ_{bulk} dominates the total electrical transport by about a factor of 300 and with this the contribution of S_{SS} is negligible. If the Dirac point were situated in the bulk band gap, i.e., available in Bi_2Se_3 and Sb_2Te_3, the electronic thermoelectric transport would most probably enhanced be with respect to bulk behavior. In Bi_2Te_3 such an enhancement is suppressed by the energetic position of the Dirac point, buried deep inside the bulk valence bands.

We furthermore note that the thermodynamical limit $S_{\text{SS}}(T \to 0) \to 0$ is reached as soon as the temperature-dependent chemical potential at zero temperature is not identical to the Dirac energy, i.e., $\mu(T = 0) \neq E_{\text{D}}$. This is emphasized in Fig. 3(f) (blue thin dotted line) for a slightly smaller p doping of $p = 3 \times 10^{20}$ cm^{-3}. Here, $\mu(T = 0) = E_{\text{D}} + 15$ meV and the thermopower of the surface state vanishes at zero temperature. The total thermopower S_{tot} of the thin film must always vanish at zero temperature, regardless of the temperature dependence of the surface states' contribution [cf. Figs. 3(d)–3(f)].

In conclusion, we presented *ab initio* calculations of the thermoelectric properties of Bi_2Te_3 films. The contributions of bulk and surface states to the conductivity and thermopower are separated by a special projection technique. The contribution of the topological surface state is particularly pronounced in the low-doping regime if the chemical potential lies in the bulk band gap.

The conductivity of the semiconductor Bi_2Te_3 is enhanced by a constant contribution because of the surface state and reaches values appropriate to a metallic system. The thermopower of bulk semiconductors shows a pronounced maximum as a function of temperature. The maximum value is determined by the size of the band gap. With the existence of the topological surface state this maximum value is drastically reduced towards metallic behavior. A reduction of the total thermopower has been found in various experiments on thin-film thermoelectric topological insulators, i.e., Bi_2Te_3, Sb_2Te_3, and $Bi_{(2-x)}Sb_{(x)}Te_3$, with, up to now, no clear explanation [38–40].

Consequently, the measured thermopower can be used to prove whether a surface state exists and contributes to the transport properties. To clearly distinguish between a topological surface state and a trivial surface state, we suggest measurements of the thermopower of a single crystal. The contribution of the topological surface state is expected to be independent of the single-crystal orientation with respect to the current direction since the topological SS occurs on all surfaces [41], while a trivial SS is restricted to selected surfaces. Following our discussion, a reduction to metallic behavior of the thermopower and electrical conductivity is expected for all orientations of the single crystal.

ACKNOWLEDGMENTS

This work was supported by the Deutsche Forschungsgemeinschaft, SPP 1386 "Nanostrukturierte Thermoelektrika: Theorie, Modellsysteme und kontrollierte Synthese".

APPENDIX: ELECTRON-PHONON SCATTERING

Electron-phonon interactions have up to now not explicitly been taken into account in our *ab initio* calculations. The latter would most probably lead *a priori* to a $1/T$ behavior of *only* the electron-phonon contribution to the bulk total relaxation time. Moreover we used the following ansatz for first estimations.[4]

Applying Matthiessen's rule, the total electronic relaxation time, neglecting electron-electron and electron-magnon processes, reads as

$$\frac{1}{\tau} = \frac{1}{\tau_{e-\text{imp}}} + \frac{1}{\tau_{e-\text{ph}}}. \tag{A1}$$

Within our paper the total relaxation time τ was fitted to experimental transport measurements. In particular the thermopower in dependence on the electrical conductivity $S(\sigma)$ was analyzed as first suggested in Ref. [42]. The total relaxation time was found to be $\tau = 11$ fs for n- and p-doped bulk materials,

---

[3] We found additional small contributions to the surface state at energies $E \leqslant E_{\text{D}} - 250$ meV. The latter do not noticeably contribute to the thermoelectric transport even at large hole charge carrier concentrations and high temperatures and can be omitted.

[4] Unfortunately, the precise numerical determination of the electron-phonon coupling on an *ab initio* level is quite demanding for semiconducting materials. The Èliashberg function has to be determined for a rather large number of chemical potentials.

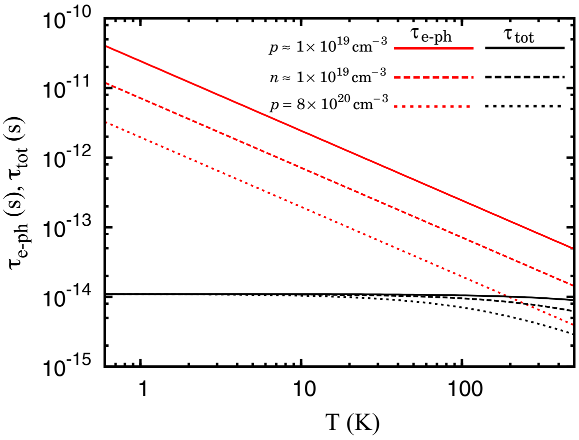

FIG. 4. (Color online) Electron-phonon contribution (red lines) to the temperature-dependent total relaxation time (black lines) of Bi_2Te_3 for different charge carrier concentrations and values of the integral electron-phonon coupling parameter λ. Further description is within the text.

which is in good agreement with other theoretically ($\tau = 6-22$ fs) [18,42] and experimentally ($\tau = 36$ fs) determined relaxation times [43]. More details can be found in a previous publication [20].

Knowing the Èliashberg function $\alpha^2\mathcal{F}(\omega)$ allows calculation of the quasielastic electron-phonon scattering rate by [44]

$$(\tau_{e-\mathrm{ph}})^{-1} = 2\pi\int_0^\infty d\omega\alpha^2\mathcal{F}(\omega)\{f^0(\epsilon_F+\hbar\omega) - f^0(\epsilon_F-\hbar\omega) + 2n^0(\omega)+1\} \overset{\epsilon_F=0}{=} 4\pi\int_0^\infty d\omega\frac{\alpha^2\mathcal{F}(\omega)}{\sinh\left(\frac{\hbar\omega}{k_BT}\right)}, \quad \text{(A2)}$$

with the coupling constant defined as

$$\lambda = 2\int\frac{\alpha^2\mathcal{F}(\omega)}{\omega}d\omega. \quad \text{(A3)}$$

Here, n^0 and f^0 are the Bose-Einstein and Fermi-Dirac distributions, respectively. Once all phonon modes can contribute to the electron-phonon scattering, i.e., $k_BT \geqslant \hbar\omega_{\max}$ (for bulk Bi_2Te_3, i.e., $\omega_{\max} \approx 17$ meV), one readily obtains the relation $\tau_{e-\mathrm{ph}} = (\frac{\hbar}{2\pi}\frac{1}{k_B\lambda})\frac{1}{T}$ from Eq. (A2) [45]. Hence, in the high-temperature limit the scattering rate becomes linear in temperature, with a slope determined only by the integral value of the electron-phonon coupling constant λ.

For strongly hole-doped bulk Bi_2Te_3 ($p = 8\times 10^{20}$ cm^{-3}; cf. Fig. 4, dotted lines) the coupling constant was estimated from the Debye temperature [46] via the McMillan formula [47] to be $\lambda \approx 0.62$. However, for smaller, thermoelectrically feasible, charge carrier concentrations (on the order of a few 10^{19} cm^{-3}) the coupling constant was very recently extracted from angle-resolved photoemission spectroscopy measurements [48]. Very small bulk contributions of about $\lambda \approx 0.05$ ($\lambda \approx 0.17$) were found for p-doped (n-doped) samples [48] (cf. Fig. 4, solid and dashed lines, respectively.). The electron-phonon coupling of the surface state is known to be very weak as well. Here, for Bi_2Te_3 values of $\lambda_{SS} \approx 0.05$ could be revealed experimentally [48] and theoretically [49,50]. These findings go along with previous similar results for the topological insulator Bi_2Se_3 ($\lambda_{SS} \approx 0.076-0.088$) [51]. To shed some light on the possible influence of electron-phonon coupling to the total relaxation time, the latter is depicted in Fig. 4 for the previously described scenarios of the electron-phonon coupling parameter λ.

With the depicted dependence of τ_{tot} and $\tau_{e-\mathrm{ph}}$, it is obvious that electron-phonon processes will not noticeably contribute to thermoelectric electron transport at room temperature and below, as the electron-phonon scattering rates are at least one order of magnitude smaller, than contributions from electron-impurity scattering. Furthermore, with the bulk contribution of the electron-phonon coupling being clearly more heavily weighted compared to the surface states' contribution, the previously discussed results on the topological surface states' signature in the thermoelectric transport still hold, while they might be even more pronounced as the ratio $\sigma_{\mathrm{SS}}/\sigma_{\mathrm{bulk}}$ increases at higher temperatures.

---

[1] H. Böttner, G. Chen, and R. Venkatasubramanian, MRS Bull. **31**, 211 (2006).
[2] G. J. Snyder and E. S. Toberer, Nat. Mater. **7**, 105 (2008).
[3] L. Fu, C. L. Kane, and E. J. Mele, Phys. Rev. Lett. **98**, 106803 (2007).
[4] H. Zhang, C.-X. Liu, X.-L. Qi, X. Dai, Z. Fang, and S.-C. Zhang, Nat. Phys. **5**, 438 (2009).
[5] M. Hasan and C. Kane, Rev. Mod. Phys. **82**, 3045 (2010).
[6] G. D. Mahan, J. Appl. Phys. **4**, 1578 (1989).
[7] Y. S. Hor, A. Richardella, P. Roushan, Y. Xia, J. G. Checkelsky, A. Yazdani, M. Z. Hasan, N. P. Ong, and R. J. Cava, Phys. Rev. B **79**, 195208 (2009).
[8] P. Ghaemi, R. Mong, and J. E. Moore, Phys. Rev. Lett. **105**, 166603 (2010).
[9] R. Takahashi and S. Murakami, Semicond. Sci. Technol. **27**, 124005 (2012).
[10] J. Henk, M. Flieger, I. V. Maznichenko, I. Mertig, A. Ernst, S. V. Eremeev, and E. V. Chulkov, Phys. Rev. Lett. **109**, 076801 (2012).
[11] Y. Ando, J. Phys. Soc. Jpn. **82**, 102001 (2013).
[12] D.-X. Qu, Y. S. Hor, J. Xiong, R. J. Cava, and N. P. Ong, Science **329**, 821 (2010).
[13] A. A. Taskin, Z. Ren, S. Sasaki, K. Segawa, and Y. Ando, Phys. Rev. Lett. **107**, 016801 (2011).
[14] I. Mertig, Rep. Prog. Phys. **62**, 237 (1999).
[15] N. Hinsche, I. Mertig, and P. Zahn, J. Phys.: Condens. Matter **23**, 295502 (2011).
[16] T. Thonhauser, T. J. Scheidemantel, J. O. Sofo, J. V. Badding, and G. D. Mahan, Phys. Rev. B **68**, 085201 (2003).
[17] B.-L. Huang and M. Kaviany, Phys. Rev. B **77**, 125209 (2008).
[18] M. S. Park, J.-H. Song, J. E. Medvedeva, M. Kim, I. G. Kim, and A. J. Freeman, Phys. Rev. B **81**, 155211 (2010).

[19] N. F. Hinsche, B. Y. Yavorsky, M. Gradhand, M. Czerner, M. Winkler, J. König, H. Böttner, I. Mertig, and P. Zahn, Phys. Rev. B **86**, 085323 (2012).

[20] N. F. Hinsche, B. Y. Yavorsky, I. Mertig, and P. Zahn, Phys. Rev. B **84**, 165214 (2011).

[21] M. Gradhand, M. Czerner, D. V. Fedorov, P. Zahn, B. Y. Yavorsky, L. Szunyogh, and I. Mertig, Phys. Rev. B **80**, 224413 (2009).

[22] S. H. Vosko and L. Wilk, Phys. Rev. B **22**, 3812 (1980).

[23] *Numerical Data and Functional Relationship in Science and Technology*, edited by O. Madelung, M. Schulz, and H. Weiss, Landolt-Börnstein, New Series, Group III, Vol. 17f (Springer, New York, 1983).

[24] S. V. Eremeev, Y. M. Koroteev, and E. V. Chulkov, JETP Lett. **91**, 387 (2010).

[25] O. V. Yazyev, J. E. Moore, and S. G. Louie, Phys. Rev. Lett. **105**, 266806 (2010).

[26] S. V. Eremeev, G. Landolt, T. V. Menshchikova, B. Slomski, Y. M. Koroteev, Z. S. Aliev, M. B. Babanly, J. Henk, A. Ernst, L. Patthey, A. Eich, A. A. Khajetoorians, J. Hagemeister, O. Pietzsch, J. Wiebe, R. Wiesendanger, P. M. Echenique, S. S. Tsirkin, I. R. Amiraslanov, J. H. Dil, and E. V. Chulkov, Nat. Commun. **3**, 635 (2012).

[27] K. Park, J. J. Heremans, V. W. Scarola, and D. Minic, Phys. Rev. Lett. **105**, 186801 (2010).

[28] C.-X. Liu, H. Zhang, B. Yan, X.-L. Qi, T. Frauenheim, X. Dai, Z. Fang, and S.-C. Zhang, Phys. Rev. B **81**, 041307(R) (2010).

[29] A. A. Taskin, S. Sasaki, K. Segawa, and Y. Ando, Phys. Rev. Lett. **109**, 066803 (2012).

[30] G. Mahan and J. Sofo, Proc. Natl. Acad. Sci. USA **93**, 7436 (1996).

[31] P. Zahn, J. Binder, I. Mertig, R. Zeller, and P. H. Dederichs, Phys. Rev. Lett. **80**, 4309 (1998).

[32] P. Zahn, N. Hinsche, B. Yavorsky, and I. Mertig, J. Phys.: Condens. Matter **23**, 505504 (2011).

[33] B. Y. Yavorsky, N. F. Hinsche, I. Mertig, and P. Zahn, Phys. Rev. B **84**, 165208 (2011).

[34] J. Henk, A. Ernst, S. V. Eremeev, E. V. Chulkov, I. V. Maznichenko, and I. Mertig, Phys. Rev. Lett. **108**, 206801 (2012).

[35] Z. Alpichshev, J. G. Analytis, J.-H. Chu, I. R. Fisher, Y. L. Chen, Z. X. Shen, A. Fang, and A. Kapitulnik, Phys. Rev. Lett. **104**, 016401 (2010).

[36] P. Roushan, J. Seo, C. V. Parker, Y. S. Hor, D. Hsieh, D. Qian, A. Richardella, M. Z. Hasan, R. J. Cava, and A. Yazdani, Nature (London) **460**, 1106 (2009).

[37] A. Hashibon and C. Elsässer, Phys. Rev. B **84**, 144117 (2011).

[38] N. Peranio, O. Eibl, and J. Nurnus, J. Appl. Phys. **100**, 114306 (2006).

[39] S. Zastrow, J. Gooth, T. Boehnert, S. Heiderich, W. Toellner, S. Heimann, S. Schulz, and K. Nielsch, Semicond. Sci. Technol. **28**, 035010 (2013).

[40] A. Boulouz, S. Chakraborty, A. Giani, F. Delannoy, A. Boyer, and J. Schumann, J. Appl. Phys. **89**, 5009 (2001).

[41] D.-H. Lee, Phys. Rev. Lett. **103**, 196804 (2009).

[42] T. J. Scheidemantel, C. Ambrosch-Draxl, T. Thonhauser, J. V. Badding, and J. O. Sofo, Phys. Rev. B **68**, 125210 (2003).

[43] M. Stordeur, M. Stölzer, H. Sobotta, and V. Riede, Phys. Status Solidi B **150**, 165 (1988).

[44] G. D. Mahan, *Many Particle Physics* (Plenum Press, New York, 1990).

[45] J. Fabian and S. Das Sarma, Phys. Rev. Lett. **83**, 1211 (1999).

[46] G. E. Shoemake, J. A. Rayne, and R. W. Ure, Jr., Phys. Rev. **185**, 1046 (1969).

[47] W. McMillan, Phys. Rev. **167**, 331 (1968).

[48] C. Chen, Z. Xie, Y. Feng, H. Yi, A. Liang, S. He, D. Mou, J. He, Y. Peng, X. Liu, Y. Liu, L. Zhao, G. Liu, X. Dong, J. Zhang, L. Yu, X. Wang, Q. Peng, Z. Wang, S. Zhang, F. Yang, C. Chen, Z. Xu, and X. J. Zhou, Sci. Rep. **3**, 2411 (2013).

[49] G. Q. Huang, Europhys. Lett. **100**, 17001 (2012).

[50] S. Giraud, A. Kundu, and R. Egger, Phys. Rev. B **85**, 035441 (2012).

[51] Z.-H. Pan, A. V. Fedorov, D. Gardner, Y. S. Lee, S. Chu, and T. Valla, Phys. Rev. Lett. **108**, 187001 (2012).